ACS Catalysis
Research Article
pubs.acs.org/acscatalysis

Preparation, Characterization, and Kinetic Study of a Core−Shell $Mn_3O_4@SiO_2$ Nanostructure Catalyst for CO Oxidation

Jing Xu, Ya-Qing Deng, Xiao-Man Zhang, Yan Luo, Wei Mao, Xue-Jing Yang, Like Ouyang, Pengfei Tian, and Yi-Fan Han*

State Key Laboratory of Chemical Engineering, East China University of Science and Technology, Shanghai 200237, China

Supporting Information

ABSTRACT: $Mn_3O_4@SiO_2$ prepared via a Stöber route showed a steady reaction rate for CO oxidation at 250 °C after 12 h. The reaction orders, with respect to CO (0.49−0.12) and O_2 (0.4−0.6), were obtained for a $Mn_3O_4@SiO_2$ catalyst ($d_{Mn_3O_4} = 7.6$ nm) in the temperature range of 220−280 °C. Via Operando Raman spectroscopy, a CO_{ad}-induced change in the symmetric stretch of Mn−O−Mn (from 636 cm^{-1} to 642 cm^{-1}) was observed for $Mn_3O_4@SiO_2$, indicating a tiny structure modification of core Mn_3O_4 by the adsorption of CO. With the combination of the catalyst structure and the kinetics of CO oxidation, we assume that this reaction proceeds mainly through the Langmuir−Hinshelwood mechanism at or below 280 °C. In comparison with the reference α-Mn_2O_3 catalyst, the presence of shell SiO_2 does not change the reaction behavior but improves the catalyst stability.

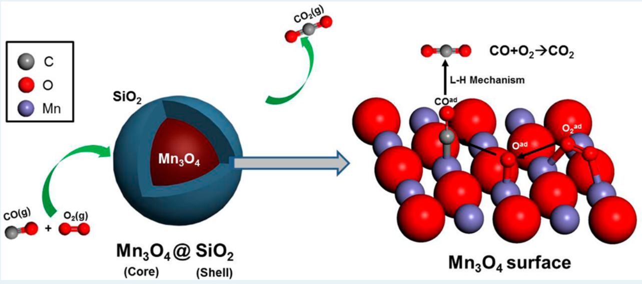

KEYWORDS: *$Mn_3O_4@SiO_2$, nanostructure catalysts, Operando Raman spectroscopy, kinetics, CO oxidation*

1. INTRODUCTION

Carbon monoxide (CO), as a main component of exhaust gas, distributes easily in air. The inhalation of CO at the ppm level is harmful to human and animal life.[1] For CO elimination, the catalytic oxidation of CO to CO_2 is still the most effective method among all approaches.[2−4] The well-known three-way catalysts for purifying exhaust gas from automobiles mainly consist of noble metals (Pt, Rh, and Pd). Tremendous efforts have been contributed to the research and development of those catalysts by improving their catalytic efficiency or exploring the reaction mechanisms.[5,6] However, the high cost of noble metals has blocked those catalysts from practical applications worldwide. Transition-metal (Ni, Cu, Mn, Co, etc.) catalysts have been found to be good alternatives toward CO oxidation,[7,8] but, compared to noble metal catalysts, show relative low reactivity and durability in the low temperature range (200−300 °C), which is also a critical zone for the cool start of automobiles[9] and is responsible for the production of ca. 90% CO in the total exhaust gas from automobiles.

Manganese oxides (MnO_x: Mn^{2+}−Mn^{7+}) and their mixtures with other oxides (CeO_2, ZrO_2, TiO_2, etc.) have proved to be highly efficient to CO oxidation[10] or VOC combustion.[11] In addition, MnO_x-based catalysts have great potential for the combustion of shale and tight gas (methane and other hydrocarbons) by reducing NO_x emission.[12] It also exhibits excellent performance for low-temperature (<200 °C) deNO_x for coal-driven power plants through selective catalytic reduction (SCR) reaction, which is usually performed at above 350 °C over various VO_x/TiO_2 catalysts.[12,13] Therefore, the development of MnO_x-based combustion catalysts is strongly desired by industry not only for pollutants abatement, but also for the utilization of fossil fuels cleanly and efficiently.

α-Mn_2O_3 has proved to be an ideal model catalyst for the fundamental study of oxidation reactions, such as low-temperature combustion of CO and VOC, because of its well-characterized structure.[14,15] More recently, several single-phase MnO_x nanostructure catalysts with high mechanical strength found to be active for CO oxidation below 350 °C.[15−18] However, the remarkable deactivation due to aggregation and phase-transformation of those catalysts is inevitable during the reaction.[7,16] To date, two strategies have been implemented for improving the durability of MnO_x-based catalysts: (i) mixing with other metal oxides to form composite oxides;[17] and (ii) confining MnO_x within a host material, so-called "nanoreactors", such as porous or tube materials, to form a core−shell composite.[18] We have demonstrated that the reactivity of Mn_3O_4 nanocrystals (ca. 7−15 nm in diameter) to CO oxidation can be greatly improved by confining those particles in a mesoporous SiO_2 (SBA-15).[19]

Nanostructure materials with a core−shell feature have been attracting worldwide attention in the fields of electronics,[20] biomedical,[21] optics,[22] catalysis,[23] and so on. A catalyst with this type of structure has a great advantage for overcoming potential sintering of core particles during the reaction. Several core−

Received: March 18, 2014
Revised: October 5, 2014
Published: October 9, 2014

shell catalysts have been examined for catalytic oxidation reactions,[24−26] which usually lead to hot spots on the catalyst surfaces. Silica is usually used as the shell, because of its chemical inertness, high thermal stability, and controllable porosity in comparison with other host materials.[27,28] However, the curiosity for the CO oxidation on MnO_x-based catalysts remains:

(1) How are the active sites originated?

(2) What is the pathway for CO oxidation over core−shell catalysts?

In this context, the controllable synthesis of Mn_3O_4@SiO_2 nanoparticles is first performed with a Stöber method, which consists of two steps: (i) the preparation of self-assembled precursor Mn_3O_4, and (ii) the polymerization of silica around Mn_3O_4 for the production of Mn_3O_4@SiO_2. Subsequently, the kinetics of CO oxidation in detail is measured using a Mn_3O_4@SiO_2 (24 h) catalyst. To further explore the structure−performance relationship of such a catalytic system, CO oxidation over Mn_3O_4@SiO_2 catalysts is evaluated in comparison with the bulk Mn_2O_3 catalyst. It is noted that α-Mn_2O_3, as a reference, shows the best activity toward CO oxidation among all bulk MnO_x (MnO, Mn_3O_4, Mn_2O_3, MnO_2) catalysts.[7]

The morphology and phase structure of Mn_3O_4@SiO_2 catalysts are characterized using transmission electron microscopy (TEM), X-ray diffraction (XRD) and N_2 adsorption. The residue organic groups in the MnO_x surface, which sources from the preparation process, is analyzed using infrared spectroscopy (IR). Later, kinetic measurements of CO oxidation are carried out in a temperature range of 200−280 °C, corresponding to the temperatures involved in the cool start of a vehicle. The structure of the near-surface phase of core Mn_3O_4 is then determined using Operando Raman spectroscopy (ORS). Other well-designed surface reactions, such as temperature-programmed surface reaction (TPSR), temperature-programmed desorption of CO and O_2 (TPD-O_2 and TPD-CO), and temperature-programmed reduction (TPR), are also performed for the determination of the Mn_3O_4 surface property. The present study will offer deep insight into the creation of active sites on Mn_3O_4 and other metal oxide catalysts with the similar structure. To the best of our knowledge, such a study has been rarely mentioned in the open literature.

2. EXPERIMENTAL SECTION

2.1. Catalyst Preparation. *2.1.1. Synthesis of Mn_3O_4 and α-Mn_2O_3 Nanoparticles.* A one-pot synthesis method is used, the details of which can be found in a previous study.[15] Manganese acetate tetrahydrate (14.7 g) and oleic acid (8.0 mL) were first dissolved in methanol (100 mL) under magnetic stirring for 1 h. The solution was then sealed in a Teflon-lined stainless steel autoclave (200 mL) and heated at 180 °C for different solvothermal times. Next, the product was dissolved into hexane, and Mn_3O_4 nanoparticles were extracted with ethanol. The brown powder product was washed with deionized water and ethanol, and then dried in air for 5 h. The as-prepared Mn_3O_4 wrapped by oleic acid was calcined in a tubular furnace in an airflow of 50 mL/min at 400 °C for 6 h. Mn_3O_4@ oleic acid nanoparticles were then prepared. The reference α-Mn_2O_3 catalyst was obtained by the calcination of the as-prepared Mn_3O_4 in a tubular furnace in an airflow of 50 mL/min at 500 °C for 10 h.

2.1.2. Preparation of Mn_3O_4@SiO_2 Nanoparticles. Mn_3O_4@oleic acid (1.0 g) was dissolved into *n*-hexane (20 mL), and then added into CTAB (100 mL, 0.05 M), using ultrasound equipment for 15 min. The resulted mixture was stirred at 25 °C until *n*-hexane was completely evaporated. Then, NaOH (1 mL, 1.0 M) was added into the solution dropwise, following by a mixture of TEOS (1 mL) and ethanol (9 mL) with the dropping rate of 1 mL/h at room temperature. The obtained brown precipitate was separated and washed with deionized (DI) water and ethanol. Finally, the resulting powder was calcined at 400 °C for 6 h. The loading amount of Mn_3O_4 is ∼20 wt % for all samples, as determined by inductively coupled plasma−mass spectrometry (ICP-MS) analysis.

2.2. Kinetic Measurements. Kinetic measurements were carried out with a micro fixed-bed reactor under differential conditions. A quartz tube with an inner diameter (ID) of 4 mm was located in a ceramic tube oven. Prior to the reaction, the catalyst was conditioned by calcining in an argon flow of 50 mL/min at 100 °C for 2 h. Reactions were carried out at a temperature range of 100−200 °C in two different atmospheres: 1.0 kPa CO, 5.0−20.0 kPa O_2, and argon (balance) and 0.1−1.0 kPa CO, 20.0 kPaO_2, and argon (balance). CO conversion was controlled below ∼10% through regulating the dilution ratio (1/100) of catalyst with α-Al_2O_3. Influent and effluent gases were analyzed with an online gas chromatograph (Shanghai Ruimin, Model GC2060) equipped with a CP-carbon BOND column. The concentrations of CO and CO_2 were determined using a methanation furnace. Each data point was taken at an interval of 2 h using high-purity gases (CO, 4.7; O_2, 5.0; H_2, 5.0; N_2, 6.0). Evaluation of the Weisz criterion showed an absence of mass-transport-related problems.[29] Furthermore, the absence of heat and mass transfer was verified experimentally by the Koros−Nowak test. The details have been described in the Supporting Information (SI). The conversion of CO was kept below 5.0% at $p_{CO} > 0.5$ kPa, and below 10.0% at $p_{CO} < 0.5$ kPa by diluting the catalyst with α-Al_2O_3, which is inert to CO oxidation under current conditions.

Absolute reaction rate (r_{CO}) of CO oxidation is expressed as shown in eq 1:

$$r_{CO}[\text{mol s}^{-1}\text{m}^{-2}{}_{\text{Me}^{-1}}] = \frac{\dot{c}_{CO,in}X_{CO}\dot{V}_{gas}}{A_{Me}} \quad (1)$$

where A_{Me} is the surface area of Mn_3O_4 in the reactor bed, $\dot{V}_{gas}$ is the total molar flow rate, X_{CO} is the CO conversion (based on CO_2 formation in the simulated reformate), and $\dot{c}_{CO}$ represent the concentrations of CO in the gas mixture (equal to p_i/p_0, where p_i is the partial pressure of reactants and p_0 is the total pressure in the system.

The calculated rates are normalized on the surface area of Mn_3O_4. For the Mn_3O_4@SiO_2 catalyst, we calculated the surface area based on a spherical model in which Mn_3O_4 is a nonporous material. For pure Mn_3O_4, the surface area is 12.8 m^2/g, as measured by the Brunauer−Emmett−Teller (BET) method.

The reaction rate was gradually decreased by ∼15% after 1000 min at 200 °C (1.0 kPa CO, 20.0 kPa O_2, balance argon). The presence of CO_2 (0.1 kPa, a maximum concentration in the reaction system) imposed no effect on the reaction rate.

2.3. Characterization. *2.3.1. X-ray Diffraction (XRD).* X-ray diffraction (XRD) patterns were recorded with a Bruker Model D8 diffractometer, using Cu Kα radiation (λ = 1.540589 Å). For comparison, a commercial α-Mn_2O_3 (Aldrich, 99.999%, 4.8 m^2/g) with an average size of 0.5 μm was analyzed as a reference. The crystal size of MnO_x was calculated with the width of diffraction profiles, referring to the full width of half-maximum (fwhm) of crystalline phase at ⟨211⟩, ⟨103⟩, and ⟨224⟩, using the Debye−Scherrer formula:

$$D = \frac{0.9\lambda}{\Delta \cos(\theta)} \quad (2)$$

where D is the crystal size, λ the wavelength of X-rays, Δ the fwhm of the diffraction peak, and θ the angle corresponding to the peak.

2.3.2. Transmission Electron Microscopy (TEM). Transmission electron microscopy (TEM) images were obtained using a JEOL Model JEM 2100 TEM system operated at 100 kV. The as-prepared Mn_3O_4@SiO_2 samples were ultrasonically dispersed in hexane and then dried over a carbon film supported on a copper grid.

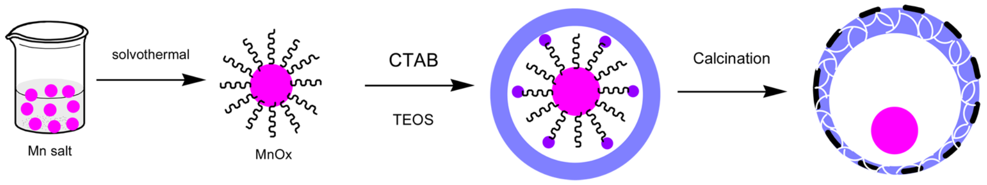

Figure 1. Synthetic scheme of core−shell catalyst structures.

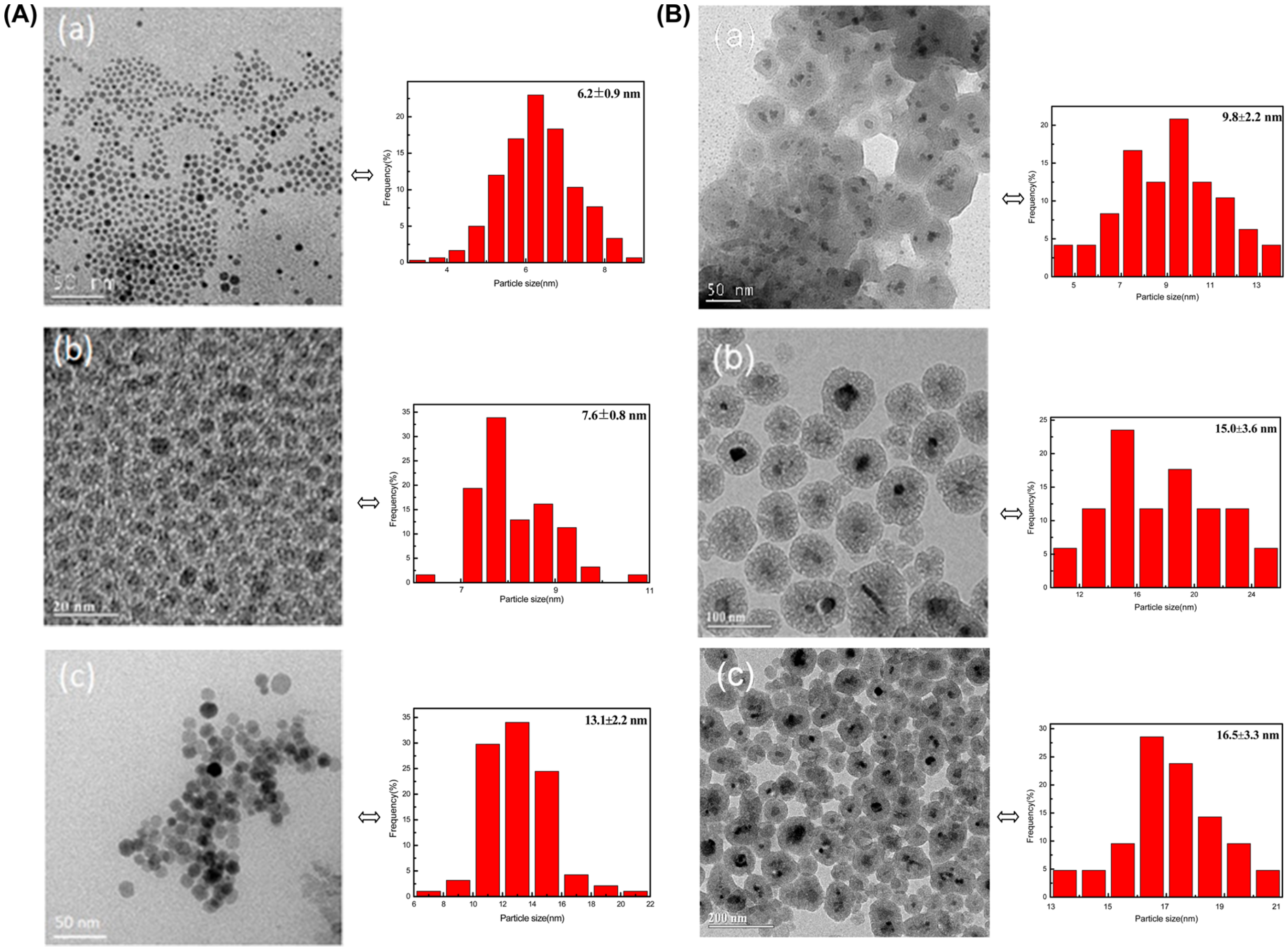

Figure 2. TEM images and particle size distribution of (A) Mn_3O_4 and (B) $Mn_3O_4@SiO_2$ nanoparticles with different solvothermal times: (a) 5 h, (b) 24 h, and (c) 48 h.

2.3.3. N_2 Adsorption−Desorption. N_2 adsorption and desorption isotherms were collected using an Autosorb-6 at −198 °C. Prior to the measurements, the samples were degassed at 300 °C until a stable vacuum of ca. 5 mTorr was reached. The silica shell has a specific surface area range 500−700 m^2/g.

2.3.4. Operando Raman Spectroscopy (ORS). Raman spectra were measured with an Operando setup using a Raman microscope (LabRAM HR, Horiba Jobin Yvon) equipped with a deep-depleted thermoelectrically cooled CCD array detector and a high-grade Leica microscope (50× long working distance objective). Sample was placed into a sample holder that was specially designed to study catalytic reactions at high temperatures and pressures (CCR1000, Linkam fitted with quartz windows). The sample was mounted on an unreactive disposable ceramic fabric filters placed inside the ceramic heating element, which is capable of heating samples from ambient up to 1000 °C. The reaction conditions are the same as that for the microfixed reactor. The carrier gases (1.0 kPa CO in Ar, 1.0 kPa CO + 20.0 kPa O_2 in argon, or argon only) were introduced into the catalyst stage via a high-pressure $^1/_{16}$-in. gas line. The gases passed through the sample and ceramic fabric filter with the flow rate of 50 mL/min. The flow rates of the reactant gases were controlled by a set of mass flow controllers. Raman measurements were performed on the same sample spot irradiated by a visible 514.5-nm Ar ion laser. The laser power from the source is normally ~30 mW. However, it should be noted that the potential heating problem induced by the laser, which usually interferes with the acquisition of the real spectroscopy, has been controlled very carefully. Thus, the laser power was minimized as much as possible, because it could be done by adjusting the laser power (using density filters) and optimizing the scanning time required without sacrificing too much, with regard to the Raman signals. It is estimated that only ~1.1 mW of the laser power reached the samples during the measurements. Therefore, *in situ* Raman signals are noisy and high precision of the peak wave numbers cannot be available. The signal for ORS was attenuated significantly above 500 °C. The scanning time for each Raman spectrum was ca. 120 s, with a spectral resolution of ~1−1.3 cm^{-1}. The temperature ramping rate was

20 °C/min when the sample was heated from 25 °C to 500 °C. Note that any structural change induced by laser was ruled out by the time-dependent spectra measured in the absence of reactant and argon. The exhaust gas was analyzed using a GC-QMS system (Model HPR-20, Hiden Analytical, Ltd.).

2.3.5. Infrared (IR) Analysis. Infrared (IR) spectroscopy was recorded on a Fourier transform infrared spectrometer (Perkin−Elmer, Model Spectrum 100). The sample was grinded to 100 mesh sieve and dried at 110 °C for 12 h to remove adsorbed water on the surface, then the sample was mixed with KBr. The semitransparent tablet was placed into the IR spectrometer for detection within a frequency range of 4000−400 cm^{-1} with a spectral resolution of 1.0 cm^{-1}.

2.3.6. CO/O_2-TPD. TPD profiles were obtained using a micro fixed-bed reactor (quartz reactor with a length of 20 cm and a diameter of 0.4 cm) connected to a GC-QMS system (Model HPR-20, Hiden Analytical, Ltd.), where masses were monitored (m/e: 18 (H_2O), 28 (CO), 32 (O_2), 44 (CO_2). All TPD experiments started with an as-prepared Mn_3O_4@SiO_2 catalyst, which was purged with argon (50 mL/min) for 10 min at 100 °C. The temperature was ramped from 25 °C to 500 °C with a rate of 20 °C/min in argon (50 mL/min).

2.3.7. Temperature-Programmed Surface Reaction (TPSR). In the same reaction system described in section 2.3.6, TPSR spectra were obtained by measuring the as-prepared Mn_3O_4@SiO_2 in a stream of 1.0% CO (with the balance being argon) with a total flow rate of 50 mL/min and a ramping rate of 20 °C/min.

2.3.7. Temperature-Programmed Reduction (TPR). Prior to the measurement, the sample (50 mg) was purged with argon at 100 °C in a flow rate of 20 mL/min for 2 h, so that most of physical adsorbed H_2O could be removed from the catalysts. The TPR was performed in a micro fixed-bed reactor that was connected to a GC-QMS system (Model HPR-20, Hiden Analytical, Ltd.), where various masses (m/e: 2, 16, 18) were monitored. The temperature was ramped from 50 °C to 800 °C with a rate of 10 °C/min in 5.0% H_2 (with the balance being argon, 50 mL/min).

3. RESULTS AND DISCUSSION

3.1. Synthesis of Mn_3O_4@SiO_2 Nanoparticles. The synthetic route for the preparation of Mn_3O_4@SiO_2 is illustrated in Figure 1. The preparation process can be briefly described as follows:

(1) manganese salt is dissolved into n-hexane solution;
(2) the precursors are bonded with long-chain templates;
(3) the cationic surfactant is then attached to the template bonded with core particles and silicon source, respectively; and
(4) finally, after hydrolysis of the silicon source, a mesoporous structure is created by burning off the template.

First, Mn_3O_4 nanoparticles were synthesized using a thermal-solvent synthesis method. The precursors resulting from different solvothermal times—5, 24, and 48 h—were bonded with oleic acid, taking on a uniform morphology with an average diameter of 6.2 ± 0.9, 7.6 ± 0.8, and 13.1 ± 2.2 nm, respectively (see Figure 2A). Then, the core particles were coated with silica through the Stöber method via the hydrolysis of TEOS in a basic solution. The template was completely burned off the mesoporous silica. Finally, the Mn_3O_4@SiO_2 core−shell nanoparticles with different thickness of the silica shells (in a range of 23−10 nm) were obtained, as evidenced by TEM images (Figure 2B). It is noted from TEM images that some SiO_2 balls are hollow without wrapping Mn_3O_4 and some core Mn_3O_4 particles aggregate during the Stöber process.

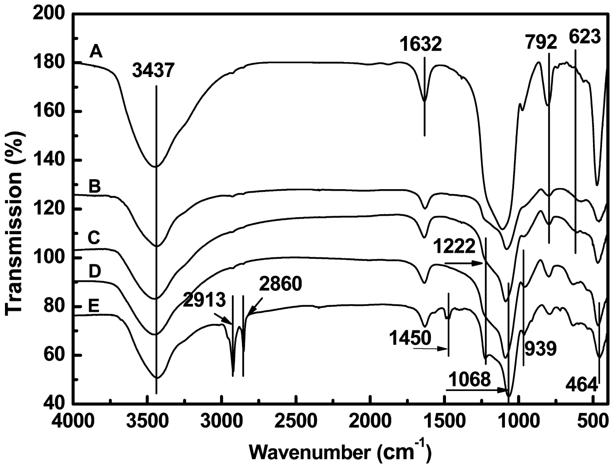

Figure 3. IR spectra of pure SiO_2 and Mn_3O_4@SiO_2 nanoparticles with different solvothermal times: (A) pure SiO_2, (B) Mn_3O_4@SiO_2 (48 h); (C) Mn_3O_4@SiO_2 (24 h); (D) Mn_3O_4@SiO_2 (5 h); (E) Mn_3O_4@SiO_2 24 h before calcination.

IR spectroscopy (Figure 3) has revealed that the peaks at 2860 and 2913 cm^{-1}, resulting from $-CH_3$ and $-CH_2$ groups, which reflect the carbon chain of the templates, disappeared completely in the final products. This observation rules out the possibility of the reaction rate being affected by residual organic groups on the surface. The bands at 464, 623, and 1222 cm^{-1} can be assigned to the distortion vibration of Mn−O bonds in an octahedral environment, Mn−O vibrations of bivalent Mn ions, and a Mn−O−Si vibration at the interface between the SiO_2 shell and the MnO_x particles, respectively.[30,31] Bands at 792 and 1450 cm^{-1} are attributed to the bending vibration of methylene and the symmetric vibration of C−O from the templates, respectively. For comparison, the IR spectrum of MnO_x-free SiO_2 was also measured. The bands at 464 and 792 cm^{-1} can be assigned to the symmetric stretching vibration of Si−O bonds. The peak at 1068 cm^{-1} is related to asymmetric stretching vibration of Si−O−Si bonds. Some overlap peaks were observed between SiO_2 shell and MnO_x particles.

In addition, it was also observed that some core particles aggregated during the fabricating process. It is difficult to obtain the core−shell structure via this method if the size of the core particles is larger than the shell chamber (e.g., core particle size >16 nm). The XRD patterns (Figure 4) showed typical Mn_3O_4 peaks at 2θ = 28.93°, 31.01°, 32.39°, 36.10°, 38.10°, 44.43°, 50.86°, 58.53°, 59.94°, and 64.57°, corresponding to the hausmannite Mn_3O_4 (JCPDS File Card No. 24-0734); while the broad peak centered at 23.0° is attributed to silica. The average particle sizes are calculated to be 5.7, 10.9, and 11.7 nm for Mn_3O_4@SiO_2 (5 h), Mn_3O_4@SiO_2 (24 h), Mn_3O_4@SiO_2 (48 h), respectively, being close to the values of 9.8, 15.0, and 16.5 nm, respectively, measured by TEM images (see Figure 2). After calcining at 400 °C, the size of core particles remained unchanged, probably because of the confined environment inside the silica shell. It is noted that one of our previous studies has demonstrated that the naked Mn_3O_4 could be transferred into α-Mn_2O_3 in the same process.[14] The TPR profiles (Figure 5) showed the sole peak ($Mn_3O_4 \rightarrow MnO$) centered at 484 °C for the as-prepared Mn_3O_4@SiO_2, being analogous with the one at 522 °C for a well-crystallized Mn_3O_4 (500 nm in diameter, Aldrich, 97.0%, 1.1 m^2/g). Meanwhile, in contrast, two peaks at 334 (α-$Mn_2O_3 \rightarrow Mn_3O_4$) and 461 °C ($Mn_3O_4 \rightarrow MnO$) were detected for the reference α-Mn_2O_3 (32 nm in diameter). Therefore, the formation of single-phase Mn_3O_4 nanocrystals inside SiO_2 spheres can be identified using a combination of TPR profiles and XRD patterns.

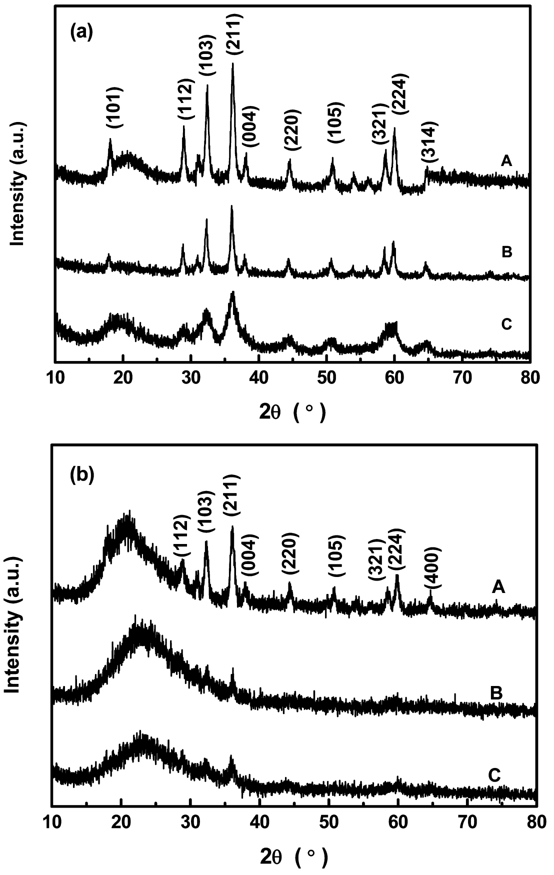

Figure 4. XRD patterns of (a) Mn_3O_4 with different solvothermal times (48 h (spectrum A), 24 h (spectrum B), and 5 h (spectrum C)); (b) $Mn_3O_4@SiO_2$ with different solvothermal times (48 h (spectrum A), 24 h (spectrum B), and 5 h (spectrum C)).

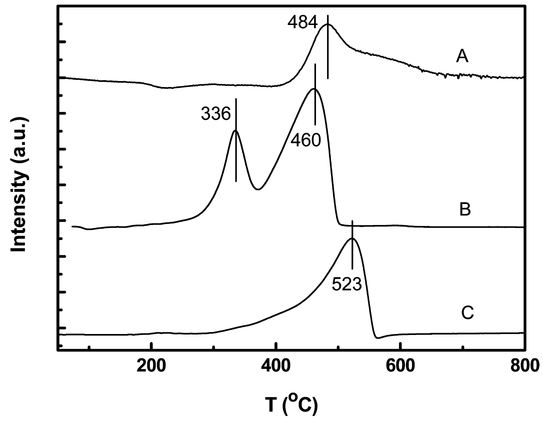

Figure 5. TPR profiles of $Mn_3O_4@SiO_2$ (24 h) (trace A), α-Mn_2O_3 (trace B), and Mn_3O_4 (trace C). The temperature was ramped from 50 °C to 800 °C with a linear heating rate of 10 °C/min in a carrier gas of H_2 (5.0 kPa + argon, 50 mL/min).

The pore volume and the surface area of these nanoparticles were determined using the Brunauer−Emmett−Teller (BET) measurement method (see Figure S1 in the Supporting Information). N_2 isothermal adsorption−desorption curves revealed that the as-prepared catalysts shared the same porous feature with the surface area of 795, 637, and 528 m^2/g for 5, 24, and 48 h, respectively. The pore distribution curves indicate that the silica spheres have a narrow pore size distribution in the range of 2−4 nm, which should be enough for free transport of the solvent, reactants, and products. The size of core particles was gradually increased with the solvothermal time, accompanied by a decrease in surface area.

3.2. Kinetics for CO Oxidation. Our previous studies have demonstrated[7] that the bulk α-Mn_2O_3 (ca. 0.5 μm) is more active than Mn_3O_4 for CO oxidation. However, with the reduction of size to the nanometer range, the reaction rate of Mn_3O_4 was observed to be higher than that of α-Mn_2O_3 in supporting catalysts.[21] Therefore, the reference α-Mn_2O_3 (ca. 30 nm in diameter) and Mn_3O_4 were used to evaluate the stability of the as-prepared catalyst. In the case of $Mn_3O_4@SiO_2$ (24 h), under the kinetic regime, the catalyst was quite stable after 12 h of reaction at 250 °C (Figure 6); while the reaction rate for the reference α-Mn_2O_3 and Mn_3O_4 catalysts decreased by ∼72% and ∼15%, respectively. Obviously, $Mn_3O_4@SiO_2$ shows excellent durability in the reaction. In the following section, in order to investigate the behavior of CO oxidation over as-prepared catalysts, kinetic measurements were performed over the $Mn_3O_4@SiO_2$ (24 h) catalyst in a water-free feed gas.

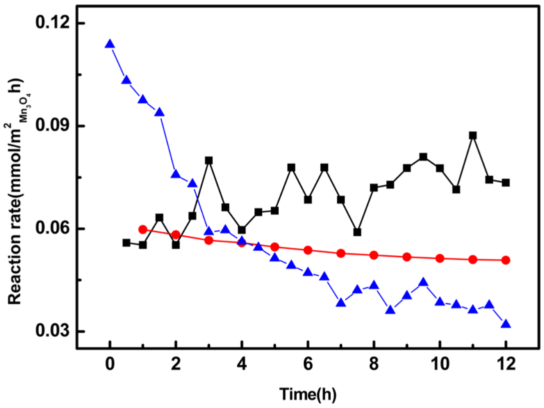

Figure 6. Stability of (▲) Mn_2O_3, (●) Mn_3O_4, and (■) $Mn_3O_4@SiO_2$ (24 h) for CO oxidation. Conditions: 1% CO, 20% O_2, balance argon; total flow rate = 50 mL/min at 250 °C, diluted with α-Al_2O_3 (1/10).

The dependence of the CO oxidation rate on p_{CO} was investigated in the partial pressure range of 0.1−1.0 kPa at 200, 220, 240, and 280 °C, respectively, at a constant p_{O_2} value (see Figure 7a). The reaction rates increased continuously with an increase in p_{CO}. The logarithmic reaction rates are proportional to the logarithmic p_{CO} over the entire pressure range investigated. Assuming a simple power law, a description of the reaction rate r_{CO} can be described as shown in eq 3:

$$\ln(r_{CO}) = \ln(k_{CO}) - \frac{E_a}{RT} + \alpha_{CO}\ln(p_{CO}) + \alpha_{O_2}\ln(p_{O_2}) \tag{3}$$

This indicates constant reaction orders α_{CO} and α_{O_2}. The α_{CO} derived from those experiments are 0.35, 0.49, 0.25, and 0.12 for 200, 220, 240, and 280 °C, respectively (see Table 1). At p_{CO} = 1.0 kPa, r_{CO} increased by a factor of ∼50 from 200 °C to 280 °C.

A similar increase in r_{CO} was observed with an increase in p_{O_2} (Figure 7b). With keeping p_{CO} = 1.0 kPa, and the reaction orders, α_{O_2} = 0.4, 0.5, 0.6, and 0.5 for 200, 220, 240, and 280 °C, respectively, were obtained from those slopes. In

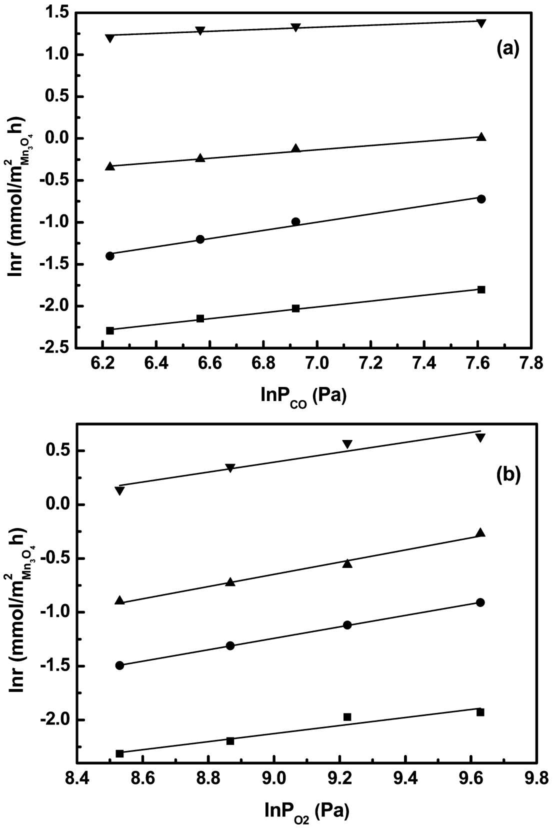

Figure 7. Dependence of reaction rate on (a) the partial pressure of CO (feed gas: 0.1−1.0 kPa CO, 20.0 kPa O_2, balance argon) and (b) the partial pressure of O_2 (feed gas: 1.0 kPa CO, 5.0−20.0 kPa O_2, balance argon). Reaction temperatures: (■) 200 °C, (●) 220 °C, (▲) 240 °C, and (▼) 280 °C. Gas hourly space velocity (GHSV) = 36 000−6000 h^{-1}. Catalyst: Mn_3O_4@SiO_2 (24 h), diluted with α-Al_2O_3 (1/100).

comparison with the reference α-Mn_2O_3 catalyst,[14] the presence of shell SiO_2 does not change the reaction behavior but does improve the catalyst stability. A similar increase in r_{CO} was measured with an increase in p_{O_2} for α-Mn_2O_3 catalyst under the same partial pressure of CO and O_2. The reaction orders, α_{O_2} = 0.4, 0.3, 0.5, 0.3, and 0.1 for 100, 130, 150, 170, and 190 °C, respectively, were obtained from kinetics measurements. The positive reaction orders with respect to CO and O_2 indicated that CO oxidation over α-Mn_2O_3 catalyst proceeds via the Langmuir−Hinshelwood mechanism. However, for α-Mn_2O_3 catalyst, the rate for CO oxidation is no longer oxygen-dependent at 190 °C, but strongly depends on p_{CO} (in other words, it is a CO-limited high-rate branch above 190 °C).

Temperature-dependent rates at p_{O_2} = 0.1, 0.2, 0.5, and 0.7 kPa were plotted with an Arrhenius diagram (Figure 8). A linear relationship between the logarithmic oxidation rates and $1/T$ was obtained for the entire temperature range, yielding E_a = 69 ± 3.0 kJ/mol. In comparison with E_a = 60 ± 2.0 kJ/mol for the reference α-Mn_2O_3 catalyst in the temperature range of 100−200 °C, the E_a value changed little for Mn_3O_4@SiO_2. All kinetic parameters, including reaction orders and apparent activation energy, are listed in Table 1; meanwhile kinetic parameters for CO oxidation over other MnO_x catalyst were also summarized for comparison.[32−37] It is noted that a rate of ∼0.046 molecule nm^{-2} s^{-1} was measured for Mn_3O_4@SiO_2 at

Table 1. Comparison of Kinetic Parameters for CO Oxidation over Various Manganese Oxide Catalysts

type of oxide	conditions	particle size (nm)	T_{100} (°C)	reaction temperature (°C)	Reaction Rate		reaction order	E_a (kJ/mol)	ref
					μmol_{CO} g^{-1} s^{-1}	molecule/(nm^2 s)			
Mn_2O_3	1% CO, 18% O_2; GHSV = 10 000 h^{-1}		200	150	N.A.	1.5		46.05	32
α-Mn_2O_3	1% CO, 20% O_2; GHSV = 36 000 h^{-1}	∼100	180	134	3.41	0.05		37.0	33
γ-Mn_2O_3	2.4% CO, 1.2% O_2; GHSV = 51 000 h^{-1}		∼500	165	4.36	N.A.			34
Mn_2O_3	2.5% CO, 2.5% O_2; GHSV = 36 000 h^{-1}	∼500			N.A.	N.A.		57.9 ± 2.0	7
Mn_3O_4	1% CO, 20% O_2; GHSV = 36 000 h^{-1}		329	230	N.A.	N.A.			35
Mn_2O_3	2% CO, 20% O_2; GHSV = 18 000−36 000 h^{-1}			210	N.A.	N.A.	α_{CO} = 0.7	61.0	36
MnO_2/SiO_2	1% CO, 1.1% O_2	∼16		200	13.3	0.03		44.6−120	37
Mn_3O_4/SBA-15	2.5% CO, 2.5% O_2; GHSV = 6000−3600 h^{-1}			230	1.66	N.A.		54.3 ± 2.0	19
α-Mn_2O_3	1% CO, 20% O_2; GHSV = 36 000 h^{-1}; 100→190 °C	32	330	153	6.44	0.14	α_{CO} = 0.4→0.8; α_{O_2} = 0.4→0	60.0 ± 2.0	14
Mn_3O_4@SiO_2 (24 h)	1% CO, 20% O_2; GHSV = 36 000 h^{-1}; 200→280 °C	8.5/25.6	270	230	2.26	0.046	α_{CO} = 0.5→0.12; α_{O_2} =0.4−0.5	69 ± 3.0	this work

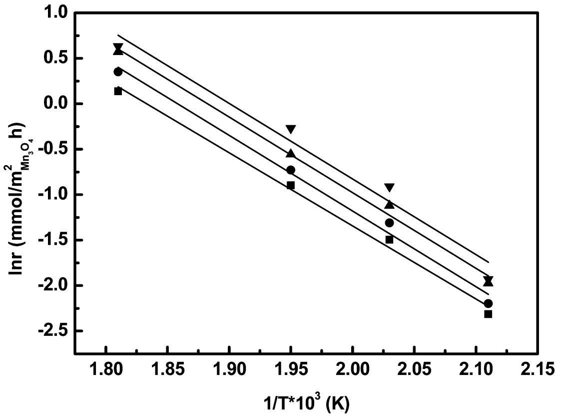

Figure 8. Arrhenius diagram of CO oxidation at different partial pressures of O_2. Feed gas: (■) 1.0 kPa, (●) 5.0 kPa, (▲) 7.0 kPa, (▼) 15.0 kPa O_2, 1.0 kPa CO, balance argon. GHSV = 36 000–6000 h^{-1}. Catalyst: Mn_3O_4@SiO_2 (24 h), diluted with α-Al_2O_3 (1/100).

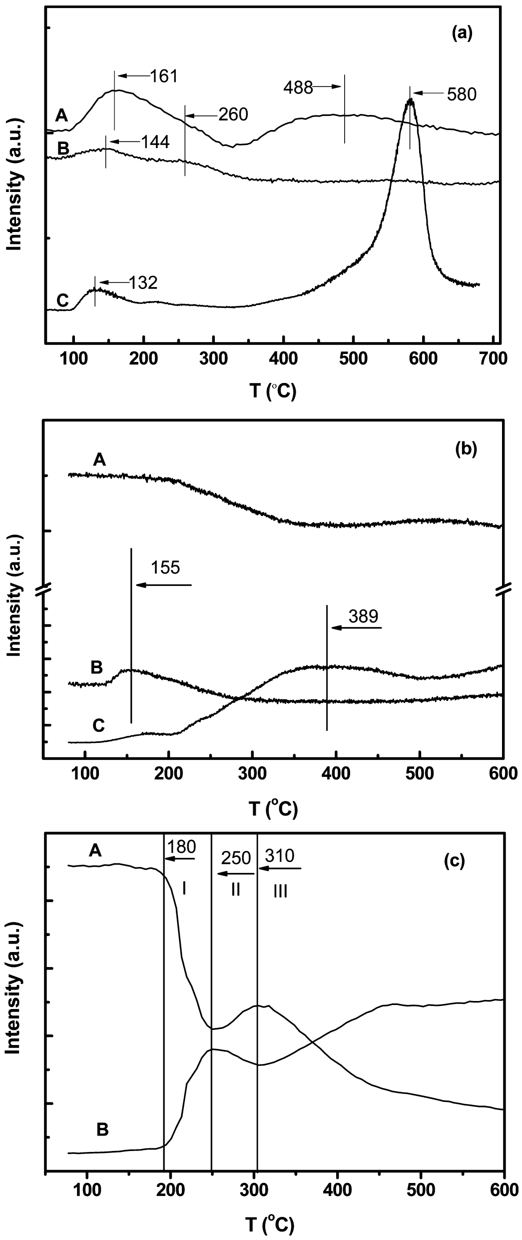

Figure 9. (a) The O_2-TPD profiles in a 20% O_2 flow (O_2 in argon) of 50 mL/min with a ramping rate of 20 °C/min: Mn_3O_4@SiO_2 (24 h) (trace A), Mn_3O_4 (trace B), and α-Mn_2O_3 (trace C). (b) The CO-TPD profiles over Mn_3O_4@SiO_2 (24 h) in a 1% CO flow (CO in argon) of 50 mL/min with a ramping rate of 20 °C/min: CO (trace A), O_2 (trace B), and CO_2 (trace C). (c) TPSR of CO oxidation profile over Mn_3O_4@SiO_2 (24 h) in a 1.0% CO flow (CO in Ar) of 50 mL/min with a ramping rate 20 °C/min: CO (trace A) and CO_2 (trace B).

230 °C, which is lower than the value measured for the reference α-Mn_2O_3 (0.14).

3.3. Temperature-Programmed Profiles.

To further illustrate the adsorption property of Mn_3O_4@SiO_2 catalysts, O_2/CO-TPD were performed. The O_2-TPD profile (spectrum A in Figure 9a) reveals there are at least two types of oxygen for the Mn_3O_4@SiO_2 catalysts: the adsorbed oxygen at 161/260 °C and the lattice oxygen at 488 °C. However, the O_2-TPD profile obtained for Mn_3O_4 catalyst (spectrum C in Figure 9a) only exhibits two weak peaks at 141 and 260 °C, respectively. In addition, for α-Mn_2O_3 catalysts, we found a desorption peak of O_2 with a strong intensity from lattice oxygen at 580 °C besides adsorbed oxygen at 132 °C.

The CO-TPD profile (Figure 9b) shows that there is no clear CO desorption peak but a broad CO_2 peak centered at 150 °C. In the meantime, a tiny O_2 desorption peak at 170 °C and a broad peak centered at 350 °C were observed. The first peak should be attributed to weakly adsorbed O_2 and the second one arose from the desorption of lattice oxygen. It is analogous with the results observed for the reference α-Mn_2O_3.[15] Likely, the core–shell structure does not change the CO adsorption on MnO_x. Moreover, the CO_2 peak at 150 °C may result from the surface reaction of $CO_{ad} + O_{ad} \rightarrow CO_2$. In order to investigate the interaction between CO_{ad} and $O_{lattice}$, a TPSR profile of CO + $O_{lattice}$ was obtained for a fresh catalyst in a stream of 1.0 kPa CO + argon. the formation of CO_2 started at ca. 180 °C, whereas no gaseous O_2 could be detected (Figure 9c). It is noted that the production of CO_2 occurred in three temperature regions: 180–250 °C (I), 250–310 °C (II), and >310 °C (III). Region I results from the reaction of CO_{ad} + O_{ad}, regions II and III may be due to the reaction of CO_{ad} with lattice oxygen from the surface phase ($O_{lattice,surf}$) and bulk ($O_{lattice,bulk}$) Mn_3O_4, respectively. Furthermore, in order to determine the potential thermal- and reactant-induced structure-modification of core Mn_3O_4 during the reaction, ORS analysis was employed.

3.4. Operando/*In Situ* Raman Spectroscopy.

The hausmannite Mn_3O_4 has a tetragonal spinel structure with a space group $I4_1/amd$ (D_{4h}^{19}). The factor-group analysis predicts 14 Raman-active modes ($2A_{1g} + 2B_{1g} + 4B_{2g} + 6E_g$).[38] This compound is highly stable under the laser beam. Therefore, the potential laser-induced structure change can be safely ruled out. Raman spectra (Figure 10a) were recorded in an argon flow by varying the temperature, from 25 °C, to 500 °C, then back to 25 °C. The bands at 343, 490, and 636 cm^{-1} can be attributed to the out-of-plane bending modes of MnO_x, the asymmetric stretch of bridge oxygen species (Mn–O–Mn), and the symmetric stretch of Mn_3O_4 groups, respectively.[7,19,27,39,40] The distinct band at 650 cm^{-1} for the bulk Mn_3O_4[38] shifted to 636 cm^{-1} for the Mn_3O_4@SiO_2 sample. All those bands, except for the one at 978 cm^{-1}, did not change during the heating process. The band at 978 cm^{-1} is usually assigned to the symmetric/asymmetric stretch of terminal Mn=O groups, indicating the existence of numerous isolated

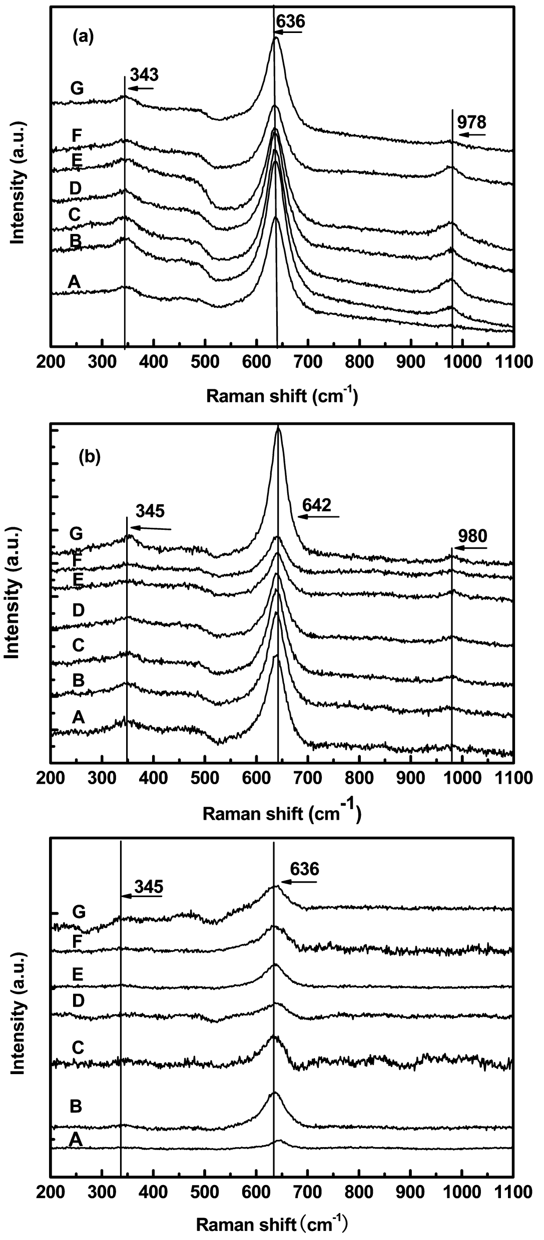

Figure 10. (a) The *in situ* Raman spectra of $Mn_3O_4@SiO_2$ (24 h) in 50 mL/min argon at different temperatures; (b) the *in situ* Raman spectra of $Mn_3O_4@SiO_2$ (24 h) in a 1% CO flow (CO in argon) of 50 mL/min at different temperatures; and (c) the Operando Raman spectra of $Mn_3O_4@SiO_2$ (24 h) in a stream of CO (1.0%), O_2 (20%), and argon (balance) with a flow rate of 50 mL/min at different temperatures: 25 °C (spectrum A), 100 °C (spectrum B), 200 °C (spectrum C), 300 °C (spectrum D), 400 °C (spectrum E), 500 °C (spectrum F), and back to 25 °C (spectrum G).

Mn_3O_4 groups; a similar species was reported to be the highly dispersed Mn_3O_4 nanocrystals in SBA-15.[38] Raman spectra were subsequently recorded in a stream of 1.0 kPa CO in argon following the same process (Figure 10b). Interestingly, the upshift of the primary band from 636 cm^{-1} to 642 cm^{-1} was observed, probably indicating that the Mn−O−Mn vibrations at the surface phase of Mn_3O_4 is interfered by the adsorption of CO. However, this band shifted to 636 cm^{-1} again with switching into reactants of 1.0 kPa CO, 20.0 kPa O_2 (Figure 10c), reflecting only a few CO_{ad} on the surface, because of the competitive adsorption between CO and O_2. The similar phenomenon has also been observed for the reference α-Mn_2O_3 catalyst in CO oxidation/adsorption.[15,16] The study of insightful mechanism of the interaction between CO and MnO_x is still ongoing in this group.

3.5. The Formation of Active Sites and Plausible Mechanisms for CO Oxidation. IR spectroscopy (Figure 3) revealed that the long carbon chain template could be completely removed, because two peaks at 2860 and 2913 cm^{-1} (corresponding to $-CH_3$ and $-CH_2$ groups, respectively) disappeared after calcination. However, some fragments of carbon chain from oleic acid were still observable, and the effects of those species on the catalyst performance were also evaluated. It was found that the CO conversion decreased by up to 22% after burning off all the carbon chain when TPSR was operated (see Figure S2 in the SI). Furthermore, only a mixture of Mn_3O_4 and Mn_2O_3 was obtained after calcining the naked core Mn_3O_4 at 400 °C, and Mn_3O_4 could be gradually transferred to α-Mn_2O_3 at 500 °C. The Mn cations in manganese oxides have three chemical states: Mn^{2+}, Mn^{3+}, and Mn^{4+}.[41]

In the presence of a SiO_2 shell, the structure of core Mn_3O_4 is unaltered, even calcined at 500 °C. Obviously, the oxidization process $Mn_3O_4 \rightarrow Mn_2O_3$ could be depressed, because of two factors: (1) the diffusion of oxygen was depressed in the confined space; (2) there are more corns and edges in those highly dispersed Mn_3O_4, as indicated by the Raman band at 978 cm^{-1} (Figure 10), so part of those sites can strongly interact with SiO_2 by forming Mn−O−Si, as identified by the IR band at 1222 cm^{-1} (Figure 3), which may prevent Mn_3O_4 from oxidizing. It may explain the improvement of stability for $Mn_3O_4@SiO_2$. Meanwhile, those species may be also responsible for the relatively lower reaction rate for $Mn_3O_4@SiO_2$, compared with the reference α-Mn_2O_3 catalyst (Table 1).

The profile of temperature-dependent CO oxidation (Figure S3 in the SI) showed that the catalytic activity varied in an order of $Mn_3O_4@SiO_2$ (24 h) > $Mn_3O_4@SiO_2$ (48 h) > $Mn_3O_4@SiO_2$ (5 h) up to the solvothermal time. In order to investigate the water effects, which is potentially encountered in practical application, ca. 12% of the CO oxidation rate over $Mn_3O_4@SiO_2$ (24 h) was lost at 300 °C under a simulated automotive exhaust gas stream containing 10 vol % H_2O.[42] A similar negative effect of H_2O on CO oxidation was also reported for $CuO-CeO_2$ catalysts[43] and RuO_2 catalysts.[44] However, a certain amount of H_2O in the feed gas has been proven to enhance low-temperature CO oxidation on metal-oxide-supported gold clusters.[45,46] To further identify the H_2O effect on $Mn_3O_4@SiO_2$, the temperature-dependent water−gas shift reaction (WGSR) was carried out in a stream consisting of 1.0 kPa CO, 10.0 kPa H_2O, and the balance being argon. Interestingly, the low WGSR rate (a rate of 0.048 molecule nm^{-2} s^{-1}) at 250 °C and 10.70 molecule nm^{-2} s^{-1} at 700 °C) was observed for $Mn_3O_4@SiO_2$ (Figure S4 in the SI), or, in other words, WGSR unlikely occurs during CO oxidation.

Kinetic measurements in the temperature range of 200−280 °C were performed by changing the partial pressure of CO and O_2. The reaction orders with respect to CO are positive, and the highest value of 0.49 was detected at 220 °C. The bond of $CO-MnO_x$ is weak at low temperatures, indicating that the CO coverage on the catalyst surface should be contingent to temperature. α_{CO} decreased to 0.1 at 280 °C, reflecting that the reaction rate becomes less dependent on gaseous CO concentration with an increase in temperature; in other words, CO_{ad} is transferred immediately by reacting with both weakly adsorbed oxygen and lattice oxygen of core Mn_3O_4, respectively, in accordance with the TPSR profiles. Similarly, positive values of α_{O_2} were observed as well. In the temperature range of 200−280 °C, the reaction orders are stable at a value of 0.5 ± 0.1. Therefore, we assume that the oxygen coverage on the catalyst surface is an important factor for CO oxidation.

The CO oxidation rate is described as

$$\ln(r_{CO}) = \ln(k_{CO}) - \frac{69}{RT} + (0.12\text{–}0.49)\ln(p_{CO}) + (0.4\text{–}0.6)\ln(p_{O_2})$$

Reaction orders with respect to CO and O_2 are both positive, suggesting that CO oxidation in the temperature range of 200−280 °C proceeds mainly through the Langmuir−Hinshelwood mechanism, whereas CO_{ad} and O_{ad} interact on the Mn_3O_4 surface. Table 1 indicates that the reaction orders, with respect to CO (0.12−0.49) over Mn_3O_4@SiO_2, are close to those values (0.4−0.8) over other MnO_x catalysts. In addition, the E_a value of 69 ± 3.0 kJ/mol over Mn_3O_4@SiO_2 is similar to the published data from other MnO_x catalysts (60 ± 2.0 kJ/mol for α-Mn_2O_3 and 54.3 ± 2.0 kJ/mol for Mn_3O_4/SBA15). Therefore, the behavior of CO oxidation over Mn_3O_4@SiO_2 changes little, in comparison with that for other MnO_x catalysts under similar reaction conditions.

On the other hand, the ORS analysis (Figure 10) shows that the vibration of Mn−O−Mn in Mn_3O_4 remains unchanged with an increase in temperature during the reaction. This fact suggests that the framework of core Mn_3O_4 is quite stable, compared to the naked α-Mn_2O_3,[15] but the reason is still unclear. As a summary, with the combination of TRSR profiles, ORS, and kinetics, we assume that the reaction may proceed through two pathways: (i) CO_{ad} is directly reacted with O_{ad} to form CO_2, $CO_{ad} + O_{ad} \rightarrow CO_2$; (ii) CO_{ad} is reacted with $O_{lattice}$ on the surface, which is quickly compensated by O_{ad}, $CO_{ad} + O_{lattice} \leftrightarrow O_{ad} \rightarrow CO_2$. However, for the time being, the structure-change due to the loss of $O_{lattice}$ during the reaction occurs too fast to be followed by Raman spectroscopy or other techniques.

4. CONCLUSIONS

A Mn_3O_4@SiO_2 catalyst was prepared with a Stöber method, while the size of core Mn_3O_4 was controlled from 5.4 nm to 15.3 nm by changing the solvothermal time. The Operando Raman spectroscopy (ORS) and the profiles from temperature-programmed techniques have demonstrated that the framework of core Mn_3O_4 could be slightly modified by the adsorption of CO. The kinetics of CO oxidation and ORS/*in situ* Raman spectra suggests that the Langmuir−Hinshelwood mechanism is possibly responsible for this reaction. The presence of SiO_2 shell does not change the behavior for CO oxidation over core Mn_3O_4 but remarkably improves its stability. Mn_3O_4@SiO_2 catalysts are promising candidates for practical application for the removal of CO under mild reaction conditions.

■ ASSOCIATED CONTENT

Supporting Information

N_2 adsorption−desorption curves for Mn_3O_4@SiO_2 catalysts, temperature-dependent CO oxidation for Mn_3O_4@SiO_2 before and after burning off residue carbon fragment, CO oxidation activity of Mn_3O_4@SiO_2 prepared by varying solvothermal time and the activity of water−gas shift reaction for Mn_3O_4@SiO_2 (24 h) catalyst are presented in the Supporting Information. This material is available free of charge via the Internet at http://pubs.acs.org.

■ AUTHOR INFORMATION

Corresponding Author

*Tel.: +86-21-64251928. Fax: +86-21-64251928. E-mail: yifanhan@ecust.edu.cn.

Notes

The authors declare no competing financial interest.

■ ACKNOWLEDGMENTS

The authors are grateful for the support from the National Science Foundation (Nos. 21176071, 21106041, 21273070), the Program for New Century Excellent Talents in University (No. NCET-12-0852), Science and Technology Commission of Shanghai Municipality (No. 11JC1402700), and the Chinese Education Ministry 111 Project (No. B08021).

■ REFERENCES

(1) Ernst, A.; Zibrak, J. D. *New Engl. J. Med.* **1998**, *339*, 1603−1608.

(2) Chen, M. S.; Cai, Y.; Yan, Z.; Gath, K. K.; Axnanda, S.; Goodman, D. W. *Surf. Sci.* **2007**, *601*, 5326−5331.

(3) Min, B. K.; Friend, C. M. *Chem. Rev.* **2007**, *107*, 2709−2724.

(4) Freund, H.-J.; Meijer, G.; Scheffler, M.; Schlögl, R.; Wolf, M. *Angew. Chem., Int. Ed.* **2011**, *50*, 10064−10094.

(5) Liu, K.; Wang, A.; Zhang, T. *ACS Catal.* **2012**, *2*, 1165−1178.

(6) Günay, M. E.; Yildirim, R. *ChemCatChem* **2013**, *5*, 1395−1406.

(7) Ramesh, K.; Chen, L.; Chen, F.; Liu, Y.; Wang, Z.; Han, Y.-F. *Catal. Today* **2008**, *131*, 477−482.

(8) Xie, X.; Li, Y.; Liu, Z.-Q.; Haruta, M.; Shen, W. *Nature* **2009**, *458*, 746−749.

(9) Wang, W.; McCool, G.; Kapur, N.; Yuan, G.; Shan, B.; Nguyen, M.; Graham, U. M.; Davis, B. H.; Jacobs, G.; Cho, K.; Hao, X. *Science* **2012**, *337*, 832−835.

(10) Cimino, S.; Colonna, S.; De Rossi, S.; Faticanti, M.; Lisi, L.; Pettiti, I.; Porta, P. *J. Catal.* **2002**, *205*, 309−317.

(11) Delimaris, D.; Ioannides, T. *Appl. Catal., B* **2008**, *84*, 303−312.

(12) Smirniotis, P. G.; Peña, D. A.; Uphade, B. S. *Angew. Chem., Int. Ed.* **2001**, *40*, 2479−2482.

(13) Qi, G.; Yang, R. T. *J. Catal.* **2003**, *217*, 434−441.

(14) Xu, J.; Deng, Y.-Q.; Luo, Y.; Mao, W.; Yang, X.-J.; Han, Y.-F. *J. Catal.* **2013**, *300*, 225−234.

(15) Luo, Y.; Deng, Y.-Q.; Mao, W.; Yang, X.-J.; Zhu, K.; Xu, J.; Han, Y.-F. *J. Phys. Chem. C* **2012**, *116*, 20975−20981.

(16) Santos, V. P.; Pereira, M. F. R.; Órfão, J. J. M.; Figueiredo, J. L. *Appl. Catal., B* **2010**, *99*, 353−363.

(17) Xu, J.; Li, P.; Song, X.; He, C.; Yu, J.; Han, Y.-F. *J. Phys. Chem. Lett.* **2010**, *1*, 1648−1654.

(18) Han, Y.-F.; Chen, F.; Zhong, Z.; Ramesh, K.; Chen, L.; Widjaja, E. *J. Phys. Chem. B* **2006**, *110*, 24450−24456.

(19) Han, Y.-F.; Chen, F.; Zhong, Z.-Y.; Ramesh, K.; Widjaja, E.; Chen, L.-W. *Catal. Commun.* **2006**, *7*, 739−744.

(20) Zhang, J.; Lima, F. H. B.; Shao, M. H.; Sasaki, K.; Wang, J. X.; Hanson, J.; Adzic, R. R. *J. Phys. Chem. B* **2005**, *109*, 22701−22704.

(21) Burns, A.; Ow, H.; Wiesner, U. *Chem. Soc. Rev.* **2006**, *35*, 1028−1042.

(22) Gao, T.; Li, Q.; Wang, T. *Chem. Mater.* **2005**, *17*, 887−892.

(23) Zhong, C. J.; Maye, M. M. *Adv. Mater.* **2001**, *13*, 1507−1511.

(24) Joo, S. H.; Park, J. Y.; Tsung, C.-K.; Yamada, Y.; Yang, P.; Somorjai, G. A. *Nat. Mater.* **2009**, *8*, 126−131.

(25) Park, J.; Song, H. *Nano Res.* **2011**, *4*, 33−49.

(26) Chaudhuri, G. R.; Paria, S. *Chem. Rev.* **2011**, *112*, 2373−2433.

(27) Bernard, M. C.; Goff, A. H. L.; Thi, B. V.; de Torresi, S. C. *J. Electrochem. Soc.* **1993**, *140*, 3065−3070.

(28) Buciuman, F.; Patcas, F.; Craciun, R.; R. T. Zahn, D. *Phys. Chem. Chem. Phys.* **1999**, *1*, 185−190.

(29) Weisz, P. B.; Prater, C. D. *Adv. Catal.* **1954**, *6*, 143−196.
(30) Ozkaya, T.; Baykal, A.; Kavas, H.; Köseoğlu, Y.; Toprak, M. S. *Physica B: Condens. Matter* **2008**, *403*, 3760−3764.
(31) Ishii, M.; Nakahira, M.; Yamanaka, T. *Solid State Commun.* **1972**, *11*, 209−212.
(32) Paulus, U. A.; Wang, Y.; Kim, S. H.; Geng, P.; Wintterlin, J.; Jacobi, K.; Ertl, G. *J. Chem. Phys.* **2004**, *121*, 11301−11308.
(33) Daté, M.; Okumura, M.; Tsubota, S.; Haruta, M. *Angew. Chem., Int. Ed.* **2004**, *43*, 2129−2132.
(34) Imamura, S.; Sawada, H.; Uemura, K.; Ishida, S. *J. Catal.* **1988**, *109*, 198−205.
(35) Wang, L. C.; Huang, X. S.; Liu, Q.; Liu, Y. M.; Cao, Y.; He, H. Y.; Fan, K. N.; Zhuang, J. H. *J. Catal.* **2008**, *259*, 66−74.
(36) Lin, R.; Liu, W.-P.; Zhong, Y.-J.; Luo, M.-F. *Appl. Catal., A* **2001**, *220*, 165−171.
(37) Wang, L.-C.; Liu, Q.; Huang, X.-S.; Liu, Y.-M.; Cao, Y.; Fan, K.-N. *Appl. Catal., B* **2009**, *88*, 204−212.
(38) Wang, L.-C.; Huang, X.-S.; Liu, Q.; Liu, Y.-M.; Cao, Y.; He, H.-Y.; Fan, K.-N.; Zhuang, J.-H. *J. Catal.* **2008**, *259*, 66−74.
(39) Han, Y.-F.; Chen, L.; Ramesh, K.; Widjaja, E.; Chilukoti, S.; Kesumawinata Surjami, I.; Chen, J. *J. Catal.* **2008**, *253*, 261−268.
(40) Han, Y.-F.; Ramesh, K.; Chen, L.; Widjaja, E.; Chilukoti, S.; Chen, F. *J. Phys. Chem. C* **2007**, *111*, 2830−2833.
(41) Stobbe, E. R.; de Boer, B. A.; Geus, J. W. *Catal. Today* **1999**, *47*, 161−167.
(42) *Basics, Audi* 2012.
(43) Wang, L.-C.; Liu, Q.; Huang, X.-S.; Liu, Y.-M.; Cao, Y.; Fan, K.-N. *Appl. Catal., B* **2009**, *88*, 204−212.
(44) Bollinger, M. A.; Vannice, M. A. *Appl. Catal., B* **1996**, *8*, 417−443.
(45) Paulus, U. A.; Wang, Y.; Kim, S. H.; Geng, P.; Wintterlin, J.; Jacobi, K.; Ertl, G. *J. Chem. Phys.* **2004**, *121*, 11301−11308.
(46) Daté, M.; Okumura, M.; Tsubota, S.; Haruta, M. *Angew. Chem., Int. Ed.* **2004**, *43*, 2129−2132.